Reversible anionic redox chemistry in high-capacity layered-oxide electrodes

M. Sathiya[1,2], G. Rousse[3], K. Ramesha[4], C. P. Laisa[4], H. Vezin[5], M. T. Sougrati[2,6,7], M-L. Doublet[2,6,7], D. Foix[2,7,8], D. Gonbeau[2,7,8], W. Walker[9], A. S. Prakash[4], M. Ben Hassine[1,7], L. Dupont[1,2,7] and J-M. Tarascon[1,2,7]*

Li-ion batteries have contributed to the commercial success of portable electronics and may soon dominate the electric transportation market provided that major scientific advances including new materials and concepts are developed. Classical positive electrodes for Li-ion technology operate mainly through an insertion–deinsertion redox process involving cationic species. However, this mechanism is insufficient to account for the high capacities exhibited by the new generation of Li-rich ($Li_{1+x}Ni_yCo_zMn_{(1-x-y-z)}O_2$) layered oxides that present unusual Li reactivity. In an attempt to overcome both the inherent composition and the structural complexity of this class of oxides, we have designed structurally related $Li_2Ru_{1-y}Sn_yO_3$ materials that have a single redox cation and exhibit sustainable reversible capacities as high as 230 mA h g^{-1}. Moreover, they present good cycling behaviour with no signs of voltage decay and a small irreversible capacity. We also unambiguously show, on the basis of an arsenal of characterization techniques, that the reactivity of these high-capacity materials towards Li entails cumulative cationic ($M^{n+} \rightarrow M^{(n+1)+}$) and anionic ($O^{2-} \rightarrow O_2^{2-}$) reversible redox processes, owing to the d-sp hybridization associated with a reductive coupling mechanism. Because Li_2MO_3 is a large family of compounds, this study opens the door to the exploration of a vast number of high-capacity materials.

Rechargeable Li-ion batteries have conquered the electronics field and are regarded as the technology of choice for powering electric vehicles. Moreover, they remain promising for grid applications that could facilitate the use of renewable energy on a larger scale. For such foreseen applications, new advances in performances/safety/costs are needed[1,2], which require a better understanding of known intercalation electrode materials and/or the discovery of new materials to ensure a leap forward in performance.

Among the positive-electrode candidates used/considered at present, layered oxides (that is, $Li(Co_{1/3}Ni_{1/3}Mn_{1/3})O_2$ (NMC); refs 3,4) are most attractive owing to greater capacities (200 mA h g^{-1}) than spinels[5] or polyanionic compounds[6,7]. Similar layered oxides having Li in excess were recently reported with capacities exceeding 250 mA h g^{-1}. Such a finding has received worldwide resonance. Although many research groups can reproduce those performances, there are numerous discrepancies concerning the chemical nature of the compound, and the mechanism by which such capacities are obtained. These compounds are reported either as composite structures [$(1 - x)LiMO_2 \cdot xLi_2MnO_3$, M = Ni, Co)] (refs 8–11) made of rocksalt Li_2MnO_3 and layered $LiMO_2$ domains or as single-phase layered oxides $Li[Li_{0.2}Ni_{0.15}Mn_{0.48}Co_{0.17}]O_2$.

The structural complexity of Li_2MO_3 lies in the 1/3 substitution of M for Li from the layered $LiMO_2$ phase (Fig. 1a), so the formula can be written as $Li(Li_{1/3}M_{2/3})O_2$. Within the LiM_2 layers, lithium ions are surrounded by six M and form honeycomb patterns. The stacking of the LiM_2 layers for M = Sn (ref. 12) differs from the one for M = Ru, (ref. 13) even though both are described in the same $C2/c$ monoclinic cells. This issue has yielded a prolific but not conclusive literature so that numerous questions still remain as to the origin of the redox process. A few scenarios involving O^{2-} migration from bulk to surface[14], transition-metal cation migration from surface to bulk, reversible oxygen oxidation[15–18] and transition metal-over-oxidation have been proposed but key experiments or new approaches remain to be performed to determine which is correct. Most approaches have so far addressed the synthetic aspects of these compounds, enlisting various annealing temperatures and cooling processes as well as different reactants or many changes/combinations in the Li/Co/Ni/Mn ratio. In contrast, few attempts, if any, have addressed the problem from the structural/chemical viewpoint; that is, departing both from the $LiMO_2$ structure and from the nature of the $3d$ elements used so far. Noting the richness of the rocksalt Li_2MO_3 (M = Ti, Ru, Mn, Mo, Sn and so on) family, the $Li_2Ru_{1-x}Mn_xO_3$ solid solution was recently shown to exhibit reversible capacities exceeding 230 mA h g^{-1} (refs 17,19). However, no definite conclusion could be reached as Mn was still electrochemically active. To bypass this second redox centre issue, we decided to study the $Li_2Ru_{1-y}Sn_yO_3$ series as Sn^{4+} ($4d^{10}$) is not easily reducible into Sn^{2+}. Here we report single-phase/single-redox cation $Li_2Ru_{1-y}Sn_yO_3$ materials that exhibit reversible capacities exceeding 220 mA h g^{-1} owing to cumulative cationic and anionic reversible redox processes, as

[1]LRCS, CNRS UMR 7314, Université de Picardie Jules Verne, 80039 Amiens, France, [2]ALISTORE-European Research Institute, FR CNRS 3104, France, [3]IMPMC, CNRS UMR 7590, Université Pierre et Marie Curie UPMC Univ Paris 06, 75252 Paris Cedex 05, France, [4]CSIR Central Electrochemical Research Institute—Chennai unit, CSIR-Madras Complex, Taramani, Chennai-600 113, India, [5]Univ. Lille Nord de France, CNRS, UMR 8516—LASIR, Univ. Lille 1, F-59655 Villeneuve d'Ascq, France, [6]Institut Charles Gerhardt, CNRS UMR5253, Université Montpellier 2, 34 095 Montpellier, France, [7]Réseau sur le Stockage Electrochimique de l'Energie (RS2E), FR CNRS 3459, France, [8]IPREM/ECP (UMR 5254), University of Pau, 2 av. Pierre Angot, 64053 Pau cedex 9, France, [9]LIOX Power, 129 N. Hill Avenue, Pasadena, California 91106, USA. *e-mail: jean-marie.tarascon@sc.u-picardie.fr; jean-marie.tarascon@college-de-france.fr

827
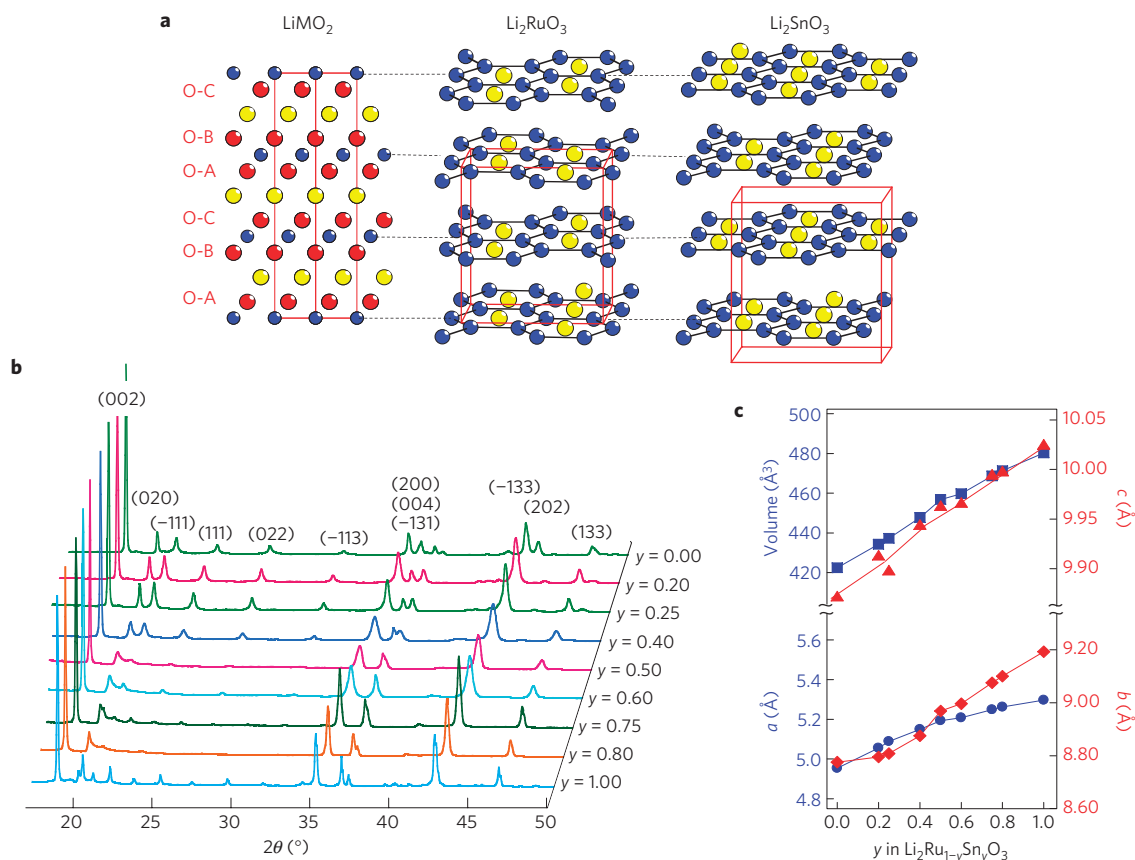
Figure 1 | Structural aspects of the $Li_2Ru_{1-y}Sn_yO_3$ solid solution. a, Structure of $LiMO_2$, Li_2RuO_3 and Li_2SnO_3. Lithium, transition-metal and oxygen atoms are yellow, blue and red respectively. For Li_2RuO_3 and Li_2SnO_3, only the LiM_2 planes are shown to see their relative stacking. The monoclinic unit cell (space group $C2/c$) is shown in red colour. **b**, XRD patterns (λ_{Cu}) of the $Li_2Ru_{1-y}Sn_yO_3$ series. Note that despite a similar metric for the unit cells, Li_2RuO_3 and Li_2SnO_3 structures differ in the repartition of the atoms among the Wyckoff sites of space group $C2/c$, leading to different stacking of the LiM_2 layers, and therefore different superstructure patterns (seen in the 2θ range [20–30°]). **c**, Lattice parameters and unit-cell volume for all of the series members (the β angle is constant for the whole series to about 99–101°).

clearly demonstrated through experimental means supported by theoretical calculations.

Members of the $Li_2Ru_{1-y}Sn_yO_3$ series were prepared through high-temperature reaction from stoichiometric amounts of RuO_2, SnC_2O_4 and Li_2CO_3 precursors, and the structures have been confirmed by X-ray diffraction (XRD; Fig. 1b). Bragg peaks shift progressively and continuously when the Sn content is increased, indicating the existence of a solid solution. The whole pattern can be indexed in the monoclinic $C2/c$ cell already reported for Li_2RuO_3 (ref. 13) and Li_2SnO_3 (ref. 12). The superstructure peaks (Fig. 1b) arising from the stacking of the honeycomb LiM_2 layers are strongly affected from $y = 0.5$ to $y = 0.8$ in the $Li_2Ru_{1-y}Sn_yO_3$ series, more likely owing to commonly observed stacking faults[20]. Last, the observed increase in the unit-cell parameters and volume with increasing y (Fig. 1c) is a direct consequence of the larger ionic radii for Sn^{4+} (0.69 Å) as compared with Ru^{4+} (0.62 Å; ref. 21).

The electrochemical performance of $Li_2Ru_{1-y}Sn_yO_3$ compounds was tested versus Li in Swagelok cells cycled between 2 and 4.6 V at a C/10 rate (Fig. 2a). Pure Li_2RuO_3 shows a staircase charge voltage profile that persists, despite being less intense, on subsequent charge–discharge cycles. The increase in Sn content ($y = 0.20$) provokes a change in the voltage–composition profile: the staircase voltage variation observed on the first charge with 3.6 and 4.25 V plateaux is replaced by an S-like variation on the subsequent discharge, and is preserved through the solid solution with polarization increasing with y. This is most likely due to electronic

limitation because Li_2RuO_3 has a semi-metal behaviour[22] whereas Li_2SnO_3 is a wide-band (3.0 eV) semiconductor[23]. In addition, the amplitude of the 3.6 V charge plateau decreases with decreasing amounts of Ru^{4+}, suggesting that it corresponds to the Ru^{4+}/Ru^{5+} redox couple (see Fig. 2a inset). Finally, regardless of the amount of carbon additive, the Li_2SnO_3 endmember shows no activity, indicating that Sn^{4+} is most likely electrochemically inactive. Once the first charge is achieved, the subsequent discharge and charge curves neatly superimpose for many cycles for all Sn-substituted compounds (see Fig. 2b for $Li_2Ru_{0.75}Sn_{0.25}O_3$). These electrodes (Fig. 2b lower inset) exhibit sustained capacity retentions with 95% of the initial capacity after 60 cycles, in contrast with the poor capacity retention measured for pure Li_2RuO_3 (Supplementary Fig. S1), suggesting a positive role of Sn for long cycle life. Last, the reversible capacities for $Li_2Ru_{1-y}Sn_yO_3$ members (blue portion, Fig. 2c) were found to slightly decrease from 250 mA h g^{-1} (pure Li_2RuO_3) with increasing Sn content. The best trade-off between performance and cycle life is achieved for $y = 0.2$–0.25. At this composition, 1.6 Li$^+$ ions can be removed from the structure during the first charge up to 4.6 V and most ($\approx$1.4) can be reinserted leading to reversible capacities reaching 230 mA h g^{-1} with limited capacity decay. Moreover, they possess reasonable rate capabilities because 90% of their initial capacity is delivered at 1C with only 10% carbon additives (Fig. 2b upper inset). Interestingly, we observed a nearly constant irreversible capacity of 0.2 Li$^+$ (Fig. 2c, green part) between the first charge and discharge whatever y and regardless of
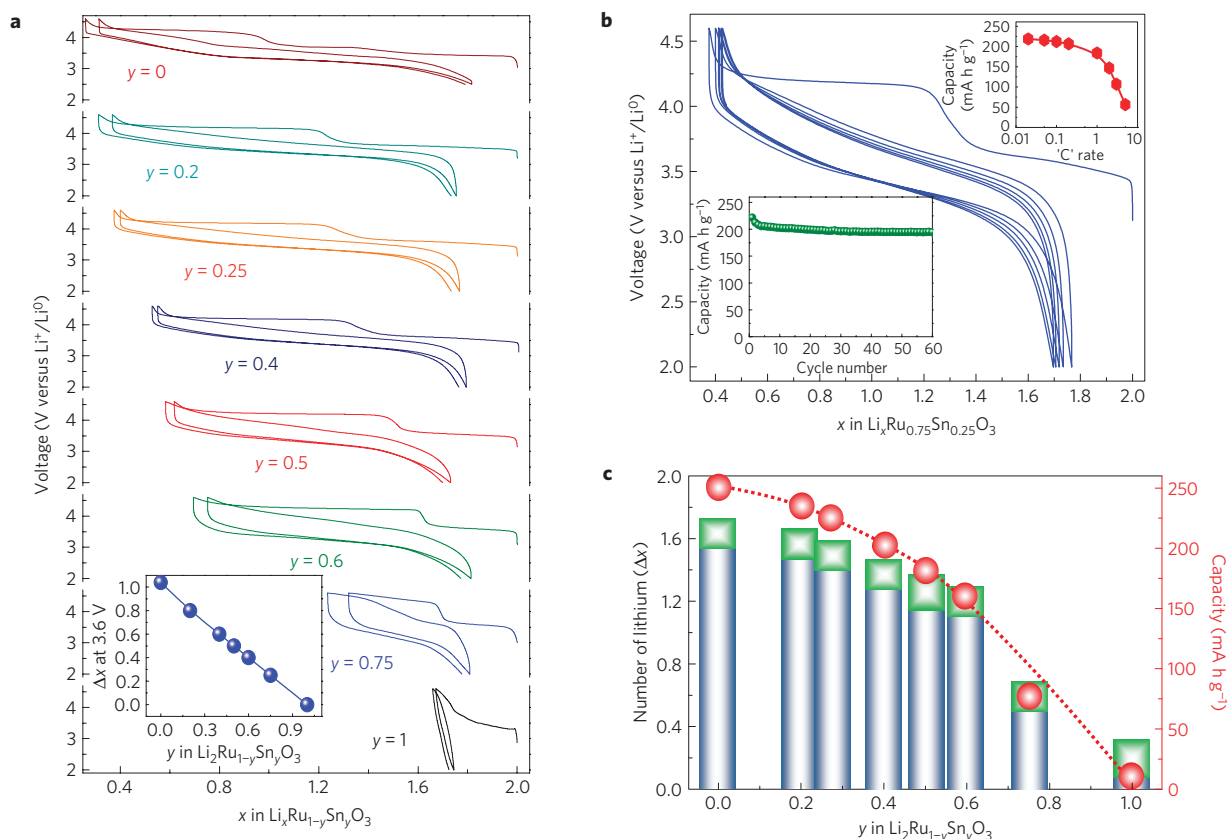
Figure 2 | Electrochemical performance of $Li_2Ru_{1-y}Sn_yO_3$. a, Voltage profile for the $Li_2Ru_{1-y}Sn_yO_3$ series, mixed with 10% Csp by weight, with (as inset) the amount of deintercalated Li on the first plateau (at 3.6 V) as a function of y. **b,** The voltage profile over several cycles for a $Li/Li_2Ru_{0.75}Sn_{0.25}O_3$ cell together with (lower left inset) its capacity retention and (top right inset) its power rate. Cells were cycled at C/10. **c,** The number of reversible (blue portion of the histogram) and irreversible (green portion of the histogram) Li^+ ions is plotted as a function of y. The total reversible capacities are shown by the red data points. The dashed red line is a guide for the eye.

the charge cutoff voltage (Supplementary Fig. S2). This reveals an irreversible phenomenon intrinsic to the material and not due to high-voltage side reactions. Its capacity, which has so far penalized the use of high-capacity Li-rich NMC phases, is here at a minimum. Nevertheless, from an application standpoint, it remains necessary to understand the origin of the voltage profile change after the first charge in $Li_2Ru_{1-y}Sn_yO_3$, which most likely deals with complex Li-driven structural and textural electrode modifications.

The lithiation–delithiation mechanism in $Li_2Ru_{0.75}Sn_{0.25}O_3$ was therefore examined by *in situ* XRD (Fig. 3a,b). Pristine $Li_2Ru_{0.75}Sn_{0.25}O_3$ presents superstructure peaks between $2\theta = 24°$ and $32°$, perfectly indexed in the $C2/c$ space group (Fig. 3c, bottom). While charging on the 3.6 V plateau, a second phase grows at the expense of the pristine one, and becomes a single phase for $x = 1.25$ ($Li_{1.25}Ru_{0.75}Sn_{0.25}O_3$) with a larger volume than the pristine one. The anisotropic change in the lattice parameters (Fig. 3d) suggests that Li ions are initially removed from the LiM_2 layers, as confirmed by density functional theory (DFT) calculations (Supplementary Table ST1). Further oxidation to $Li_{0.4}Ru_{0.75}Sn_{0.25}O_3$ (4.25 V plateau) indicates a different behaviour as the XRD peaks do not shift but broaden, indicating a loss of crystallinity without any change in the lattice parameters. This could also be interpreted as the nucleation of a new disordered phase because superstructure peaks are barely seen at the end of charge (Fig. 3c). On subsequent discharge, lattice parameters shift back continuously to their original values (Fig. 3d) but without going through a biphasic process, and superstructure peaks do not reappear.

To better assess the reason behind the changes in the intensity of the superstructure peaks through the first cycle, we studied

the $Li_2Ru_{0.75}Sn_{0.25}O_3$ electrode at various stages of reduction and oxidation by means of transmission electron microscopy (TEM) and more specially selected-area electron diffraction (SAED). Whatever the state of charge/discharge, the particles remained crystallized with their nanometric character (high-resolution TEM, Supplementary Fig. S3) accounting for the broadness of the XRD peaks. The c^* zone axis SAED pattern for pristine $Li_2Ru_{0.75}Sn_{0.25}O_3$ (Fig. 4a) presents numerous reflections, all indexed in the expected monoclinic structure. Superstructure peaks are also clearly seen from $(020)^*$ and equivalent reflections (plain green hexagonal array) that all disappear when charging to 4 V (Fig. 4b) and further to 4.6 V (Fig. 4c; only a weak ring around the transmitted beam (green arc) is still observed), in perfect agreement with the XRD observation. In addition, we note a strong increase of the $(200)^*$ and equivalent reflections (dashed green hexagonal array) that could not be spotted in XRD owing to the broadening of the peaks. On the discharged sample (Fig. 4d), $(020)^*$ and equivalent spots reappear but with a very weak intensity. To understand this inversion of intensity between $(200)^*$ and $(020)^*$ spots on the first cycle, we simulated, without success, different Li–Ru–Sn cation migration models. Shifts in the oxygen positions when Li is completely removed from the structure can better explain this intensity difference.

Whatever the origin of such inversion intensity, we have determined that once the system has fallen into this new electrochemically stabilized structure during the first cycle, it will not evolve for dozens of cycles because the SAED patterns of the discharged samples look alike. Nevertheless, after long cycling of a $Li_2Ru_{0.75}Sn_{0.25}O_3$ electrode (100 cycles), SAED patterns indicate a
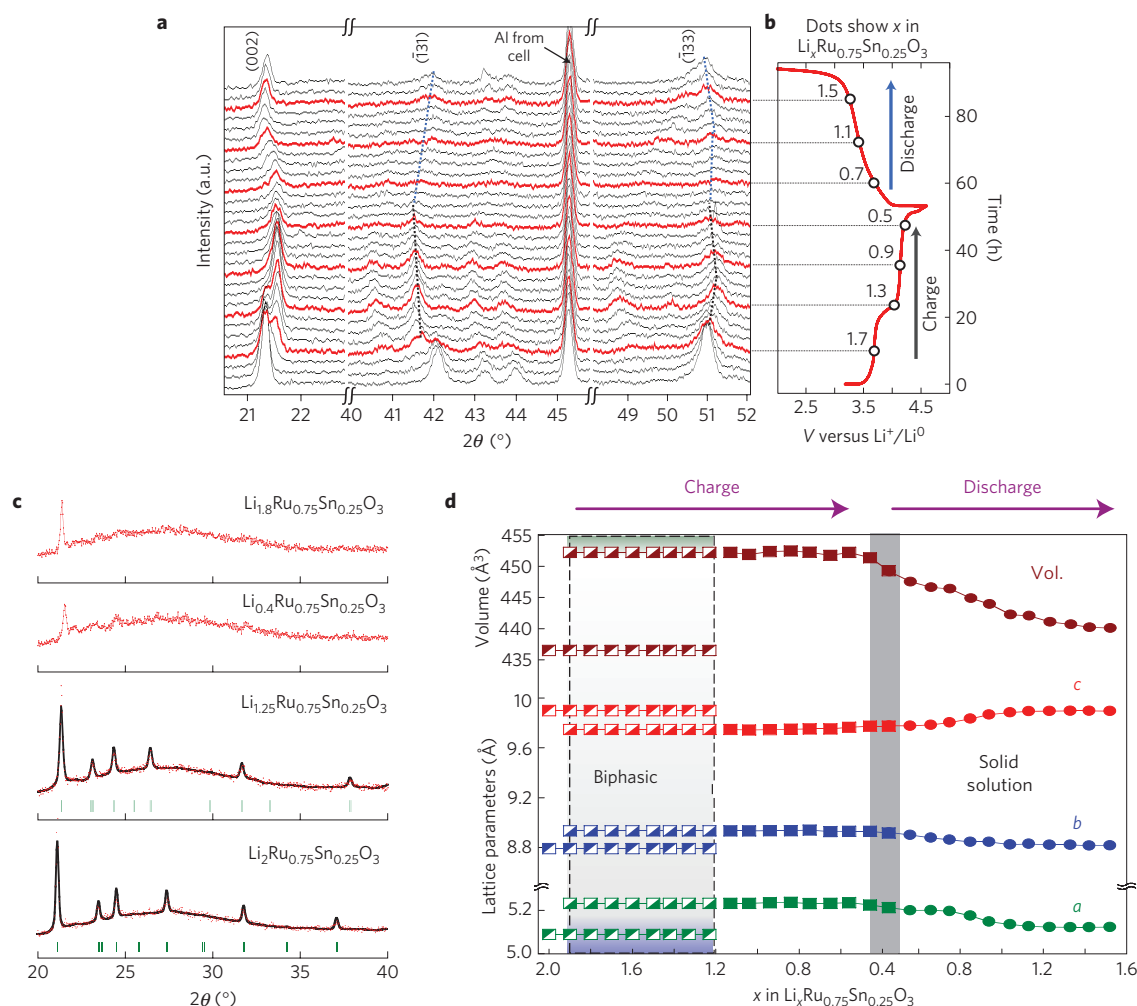
Figure 3 | Li-driven structural behaviour on cycling. a,b, The collected XRD patterns (λ_{Co}) (**a**) while a Li/Li$_2$Ru$_{0.75}$Sn$_{0.25}$O$_3$ cell is charged and discharged at a rate of C/20 (**b**). The peak at 45.3° comes from Al present in the electrochemical cell. **c,** The patterns collected for the pristine, charged to 4 V, 4.6 V and fully discharged samples issued from **a** zoomed over the $2\theta = 20$–$40°$ range, to highlight the evolution of the superstructure reflections. **d,** The lattice parameters and the unit cell volume obtained by fitting the XRD patterns from **a**. The grey vertical region around $x = 0.4$ shows the transition between the charge and discharge processes.

slight decrease of intensity for all spots, and the onset of extra dots lying on forbidden (100)* and equivalent planes (yellow arrows in Fig. 4e). This suggests a cycling-driven structural evolution, which is not surprising as the formation of spinel-like nanodomains[24,25] has been commonly observed for the high-capacity Li-rich NMC compounds and is believed to be responsible for their large voltage decay on cycling. Following the discharge voltage curves and corresponding derivative plots (dx/dV; ref. 26; Fig. 4f), minor changes in the voltage decay are observed here on cycling as opposed to marked changes for the Li-rich NMC compounds[27]. The chances of forming spinel-like domains, which require a cation to migrate through a tetrahedral site ($O_h \rightarrow T_d \rightarrow O_h$), are slim with large cations such as Sn^{4+}. Besides, only a handful of Ru- or Sn-based spinel phases (Co$_2$RuO$_4$ (ref. 28) and Cd$_2$SnO$_4$ (ref. 29)) have been reported so far. Further SAED patterns (Supplementary Fig. S4) indicate that the formation of twin domains on cycling explains our observations.

Mössbauer spectroscopy was used as an elegant method to probe the Sn local structure and redox activity. Spectra collected for Li$_2$Ru$_{1-y}$Sn$_y$O$_3$ members show a single peak (Fig. 4g) typical for Sn^{4+} in an octahedral environment as observed for BaSnO$_3$ and CaSnO$_3$ (refs 30,31). Its isomer shift ($\sim$0.15 mm s^{-1} for Li$_2$SnO$_3$) increases with the Ru content, suggesting a higher covalent character of the Ru—O bonds for the Ru-rich members (Supplementary

Table S2). In contrast, no change in the Sn isomer shift was observed on Li/Li$_2$Ru$_{0.5}$Sn$_{0.5}$O$_3$ half-cells on charge and discharge, indicating that Sn^{4+} is electrochemically inactive (Fig. 4g). Moreover, when monitoring the variation of both the quadrupole splitting and the spectrum absorption on cycling (Supplementary Fig. S5), we could respectively deduce that the first charge triggers an irreversible local structural distortion around Sn and the Sn–O bonds weaken/strengthen on Li extraction/insertion, suggesting that Sn is less bounded to the oxygen network in charged samples.

To further investigate the Li-driven redox processes, X-ray photoelectron spectroscopy (XPS) analyses were carried out for the pristine Li$_2$Ru$_{0.5}$Sn$_{0.5}$O$_3$ and for samples charged to 4 V, 4.6 V and fully discharged to 2.0 V. First, the Sn3d core spectra and more specifically the (O1s − Sn3d) binding energy difference (Supplementary Fig. S6) remain unchanged over the whole charge–discharge cycle, indicating that Sn does not participate in the redox process, in full agreement with Mössbauer results. The Ru3d core spectra (Fig. 5a) show a Ru3$d_{5/2}$ binding energy ($\sim$282.2 eV) for pristine Li$_2$Ru$_{0.5}$Sn$_{0.5}$O$_3$, consistent with Ru^{4+} (refs 32,33). When the Li$_2$Ru$_{0.5}$Sn$_{0.5}$O$_3$ electrode is charged to 4 V, the Ru3$d_{5/2}$ binding energy shifts positive by 0.7 eV, demonstrating an increase in the Ru oxidation state from Ru^{4+} to Ru^{5+}. Surprisingly, after charging at 4.6 V, a reverse evolution is observed. This could result from
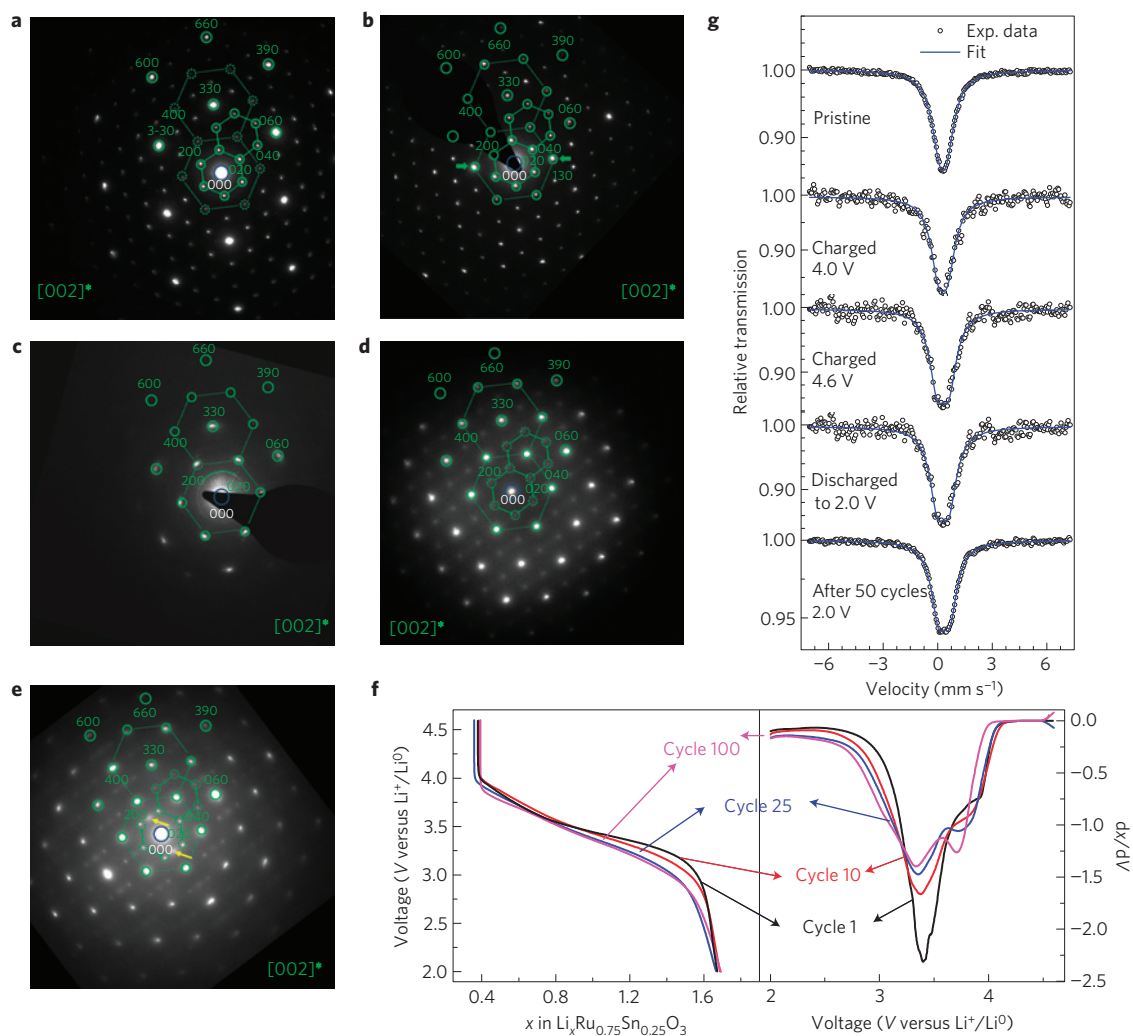
Figure 4 | Microscopy and Mössbauer measurements for spotting the evolution of $Li_2Ru_{1-y}Sn_yO_3$ electrodes on cycling. SAED patterns recorded along the same c^* zone axis at various stage of cycling. **a**, Pristine $Li_2Ru_{0.75}Sn_{0.25}O_3$ material. **b**, On the end of the 3.6 V plateau. **c**, End of charge. **d**, After 1 cycle. **e**, After the 100th discharge. The $C2/c$ cell setting was used to index spots circled in green and form two different hexagonal arrays (one made with the dashed green line; the other one with solid one). Intense reflections are circled with solid lines and weak reflections with dashed lines. **f**, Discharge curves (left) and corresponding dx/dV curves (right) after 1, 10, 25 and 100 cycles for $Li_2Ru_{0.75}Sn_{0.25}O_3$ electrodes. **g**, Room-temperature ^{119}Sn Mössbauer spectrum for pristine $Li_2Ru_{0.5}Sn_{0.5}O_3$ material (top), and in situ spectra for the same $Li_2Ru_{0.5}Sn_{0.5}O_3$ electrode charged to 4.0 V, to 4.6 V and discharged to 2.0 V. The bottom curve is an ex situ spectrum of the electrode in its discharged state, after 50 cycles.

a significant modification of the Ru environment (for example, distortion) inducing strong electronic redistributions along the Ru–O bonds. For the fully discharged sample, the $Ru3d_{5/2}$ peak shifts to lower binding energies by 0.9 eV in line with a reduction process. Pursuing further the evolution beyond the second cycle, we note practically identical results to those obtained for the first charge/discharge, indicative of a reversible redox process (Supplementary Fig. S6).

Turning to the O1s spectrum (Fig. 5b) of pristine $Li_2Ru_{0.5}Sn_{0.5}O_3$, two peaks characteristic of O^{2-} anions belonging to the crystalline network (529.5 eV peak)[34] and weakly adsorbed surface species are clearly visible. The spectrum barely changes when the sample is oxidized to 4 V but markedly changes for the 4.6 V oxidized sample with, namely, the onset of a new component at ~530.5 eV corresponding to oxide ions with a lower electronic density as compared with O^{2-} ions. This peak can be attributed to the existence of formal O_2^{2-} species or to under-coordinated oxygen atoms[34]. It disappears after the first discharge and the shape of the O1s spectrum converts back to the pristine. The component at 530.5 eV reappears/disappears on subsequent charges/discharges,

demonstrating the redox activity of oxygen. However, these repeated observations cannot ensure that it is a bulk phenomenon.

To address this remaining question, the complex Ru–O interactions spotted by XPS were further studied by electron paramagnetic resonance (EPR) for $Li_2Ru_{0.5}Sn_{0.5}O_3$. At room temperature, the pristine Ru^{4+} material (Fig. 5c) shows no signal as expected for such EPR-silent species at the X-band. In contrast, the 4 V charged sample shows the onset of a narrow isotropic line of 12 G centred at a g value (2.0003) lower than that of free electrons ($g = 2.0023$), suggesting a partial localization of the 4d electrons. For the 4.6 V sample, this line shape broadens asymmetrically, indicative of a dipolar broadening due to electron–electron interaction. Once discharged to 2.0 V, the EPR spectrum nearly converts back to the pristine one, stressing further the reversibility of the process. This room-temperature study suggests that electrons are localized close to a d orbital for the Ru^{5+} compound and jump to another localization site as the sample is fully charged in agreement with a stronger Ru(4d)–O(2p) hybridization.

Further EPR experiments were performed at 4 K to better identify the paramagnetic species. Whereas the Ru^{4+} pristine
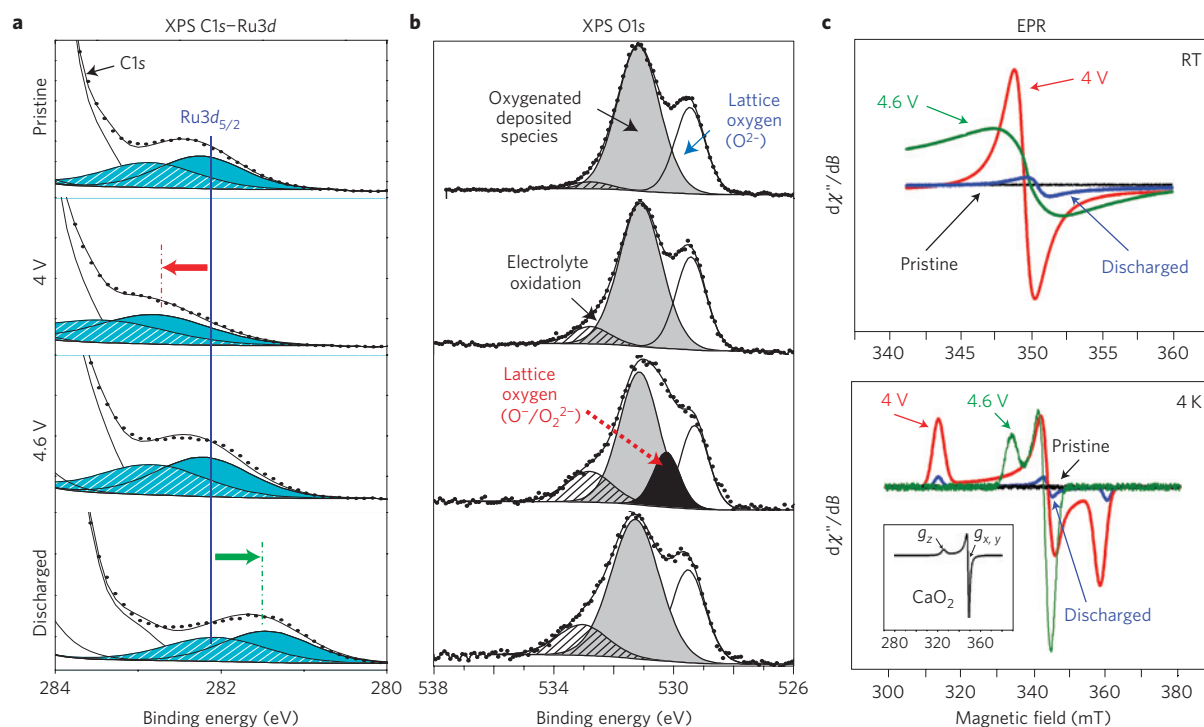
Figure 5 | Detection of anionic redox species. XPS for $Li_2Ru_{0.5}Sn_{0.5}O_3$ with, from top to bottom, the spectra collected for the pristine sample and the samples charged to 4 V, 4.6 V, and discharged to 2.0 V. **a**, $C1s$–$Ru3d$ spectra showing the $Ru3d_{5/2}$ peak at 282.2 eV (blue) associated with a spin–orbit splitting of about 4.1 eV, together with a satellite spectral feature (283.1 eV, dashed blue region). The red and green arrows show the shift of the $Ru3d_{5/2}$ peak during the charging (red) and discharging (green) processes. **b**, The O1s core spectrum with two peaks at 529.5 and 531.6 eV corresponding to O^{2-} anions belonging to the crystalline network[34] and corresponding to weakly adsorbed surface species, respectively, the latter being also responsible for the weak signal at ~533.2 eV. Note for 4.6 V spectrum (third down) the increase of the 533.2 eV component associated with oxygenated species resulting from some electrolyte oxidation[50], which then does not evolve on cycling, suggesting that surface deposits mainly occur during the first charge. **c**, X-band EPR spectra recorded on the same series at room temperature (RT; top) and 4 K (bottom). Note that Ru^{4+} (that is, integer spin ground state) is silent in the X-band. The inset shows the spectra of CaO_2 taken at 4 K under similar conditions.

material remains silent, the 4 V sample shows a signal typical of low-spin ($S = 1/2$) Ru^{5+} in a distorted bipyramidal geometry with a weak g-factor anisotropy indicative of an electronic ground state that is removed from the excited state. The most spectacular result comes from the fully charged (4.6 V) sample whose EPR signal shows an axial symmetry ($g_{\parallel} = 2.01$, $g_{\perp} = 2.004$) very close to the 4 K signal of calcium peroxide/superoxide (see inset Fig. 5c, bottom, $g_{\parallel} = 2.05$, $g_{\perp} = 2.006$; ref. 35), thus giving evidence for the formation of peroxo/superoxo-like species. Most likely, a reductive coupling mechanism takes place to stabilize the highly oxidized Ru^{6+} cation by modifying its coordination sphere into either Ru^{5+}–$(O_2)^{2-}$ or Ru^{4+}–$(O_2)^{-}$ (Fig. 6a). This hypothesis is fully confirmed by DFT calculations showing a strong distortion of the oxygen network on lithium removal and the formation of peroxo/superoxo-like species at the very end of charge (Fig. 6b). The sample spin concentration, as deduced from a double integration of the spectrum (see Supplementary Fig. S7) led us to estimate that $23\pm6\%$ of oxygen are peroxo/superoxo species. These entities should present short O–O distances that could not be pinpointed by XRD owing to the absence of long-range order.

In light of previous works[14], oxygen loss may occur in these high-capacity electrodes. *In situ* gas and pressure analyses (Fig. 6c–d) were then carried out. As the $Li_2Ru_{0.5}Sn_{0.5}O_3$ material is initially charged up to the middle of the 4.25 V plateau, neither the cell pressure nor the gas composition changes. At the very end of charge, a tiny increase in the cell pressure of ~0.1 PSI is detected. *In situ* mass spectrometry indicates that the involved gas is O_2, and different tests on blank cells confirm it comes from the cathode materials. On further cycling, the $Li_2Ru_{0.5}Sn_{0.5}O_3$ material no longer

exhibits gas evolution. Identical experiments conducted on both (Ru–Mn)-based (Supplementary Fig. S8) and Li-rich layered NMC (ref. 14) have revealed oxygen releases 3–6 times greater. Therefore, the presence of Sn, which enhances the flexibility of the M–O bonds, minimizes oxygen release[18], thus leading to small irreversible capacities (~10–12%).

Overall, a common denominator to these high-capacity $Li_2Ru_{1-y}Sn_yO_3$ and Li-rich NMC electrodes is their first charge that markedly differs from the subsequent ones. In designing materials relying on a single cationic redox centre, at present we decipher the complex Li uptake–removal mechanism through complementary analytical techniques and electrochemical measurements. During the first charge Ru^{4+} is initially oxidized (3.6 V). At higher potential (4.25 V) the nucleation of a distorted/disordered phase results in a modification of the oxygen network (favoured by the low bonding of Sn^{4+}) to form peroxo/superoxo-like species. This structure further evolves on the following discharge so that it will never recover the structure of the pristine material. From the second cycle, the system is fully reversible with capacities up to nearly twice the Ru amount in the material. This naively implies that the large reversible capacity measured in $Li_2Ru_{1-y}Sn_yO_3$ results equally from a cationic (Ru^{4+}/Ru^{5+}) and an anionic (O^{2-}/O_2^{2-}) redox process. The last notion implies that partially filled Ru($4d$) levels strongly overlap with the O($2p$) valence band, so that delithiation through the 4.25 V plateau primarily affects the O($2p$) levels, leaving holes on the oxygen anions.

Such a pronounced M(nd)–X(np) metal–ligand hybridization situation is quite common when the ligand orbitals are highly delocalized so that they form covalent bonds with the $3d$-metals
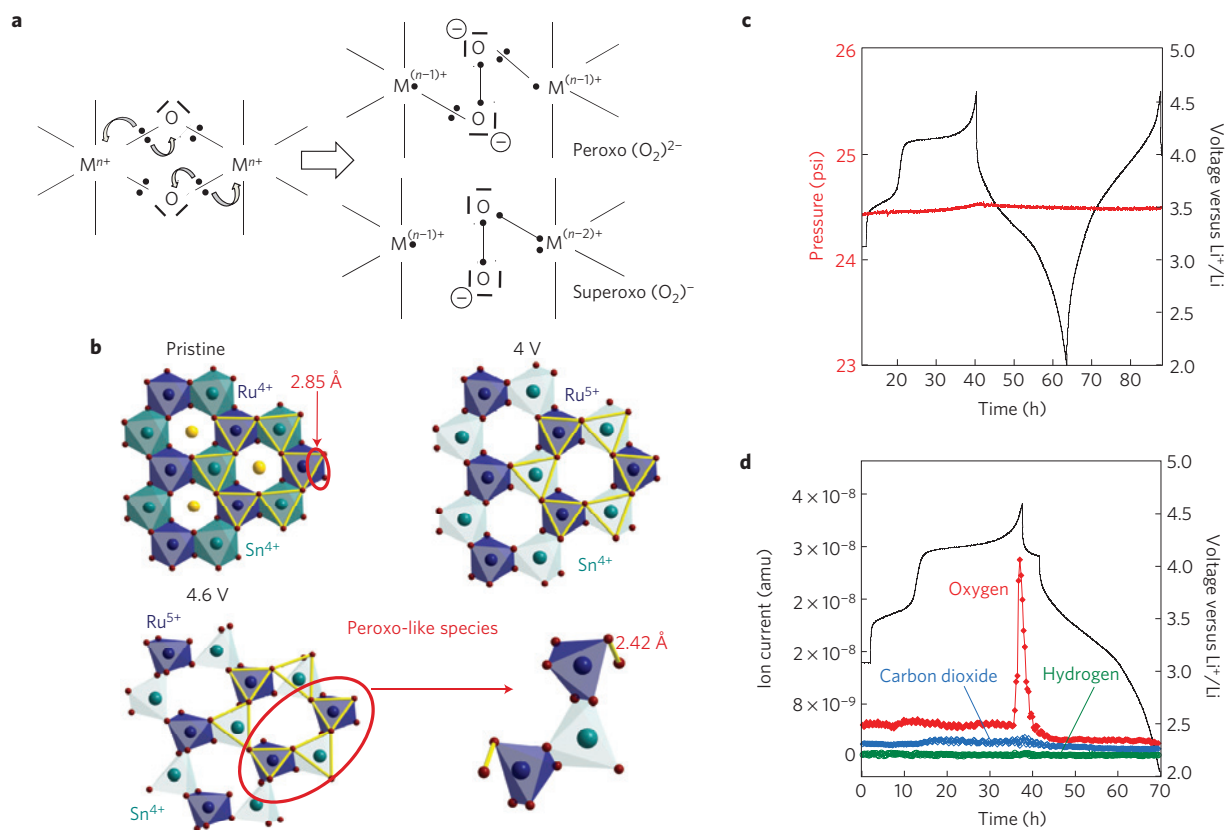
Figure 6 | Reductive coupling mechanism, calculations accounting for superoxo-like species and measured oxygen release. a, The reductive coupling mechanism of two oxo-ligands coordinated to the transition metals leads to a single or double metal reduction depending on the coordination mode of the O_2 moiety. The scheme is represented for two edge-shared MO_6 entities as they appear in the honeycomb structure of the LiM_2 layers in $Li_2Ru_{1-y}Sn_yO_3$ structures. A peroxo-like species arises from the formation of a $(O_2)^{2-}$ moiety that is coordinated to two singly reduced transition metals, that is, $M^{(n-1)+}-(O_2)^{2-}-M^{(n-1)+}$ whereas a superoxo-like species arises from the formation of a $(O_2)^-$ moiety that is now coordinated to one doubly reduced transition metal, that is, $M^{(n-2)+}-(O_2)^-$. The ability of the system to form either peroxo or superoxo species will obviously depend on the distribution of Ru/Sn in the honeycomb LiM_2 layers (that is, the number of direct nearest Ru–Ru neighbours) and therefore on the y ratio in $Li_2Ru_{1-y}Sn_yO_3$. **b**, Representation of one LiM_2 honeycomb layer of the $Li_xRu_{0.5}Sn_{0.5}O_3$ as obtained from DFT calculations after full structural relaxation for the lithium compositions $x = 2$ (pristine), 1.5 (4 V) and 0.75 (4.6 V). The Ru, Sn, O and Li atoms are represented in blue, green, red and yellow, respectively. The yellow bonds are shown to follow the distortion of the oxygen network. The SnO_6 polyhedra (dark green) are shown in light green to illustrate that Sn^{4+} is no longer bonded to the oxygen lattice once 0.5 Li are removed and can easily reorganize within the layer. The peroxo-like species are visible in the fully delithiated compound (4.6V). **c**, Oxygen pressure evolution during the first charge, first discharge and second charge for a $Li_2Ru_{0.5}Sn_{0.5}O_3$ cell. **d**, Gas profile of the first cycle for the same cell cycled at room temperature.

as for chalcogenides[36–38] or phosphides[39], but less frequent for oxides. This n_d-s_p hole redox chemistry was theoretically proposed in the late 1990s[40,41] to account for the Li deinsertion process in Li_xCoO_2 at low x. Hints of confirmation were provided by O K-edge electron energy-loss spectrometry[42] and O1s XPS core spectra measurements[43], which have revealed lower electron density on oxygen. Herein, we go beyond this phenomenon by showing that the strong destabilization associated with the creation of O^- anions triggers the formation of short O–O bonds to restabilize the oxygen network, thus leading to peroxo–superoxo species that could be spotted both by XPS and EPR and confirmed by DFT structural relaxations.

Therefore, on oxidation, the formation of $Ru^{6+}-O^{2-} \rightarrow Ru^{5+} + O^-$ species (for example, hole in the oxygen) ultimately ends by the condensation of O_2^{2-} (peroxo-like) species, instead of releasing O_2 gas, as observed in the Ru/Mn case. Such a mechanism, which explains why the reversible capacity nearly equals twice the amount of Ru atoms (within the accuracy of the measurements), is depicted in Fig. 6a. It is of great interest for large-capacity applications as it allows for an internal redox process, that is, a self-regeneration of the transition-metal oxidation state on charge, by exploiting

the ability of the ligand to adopt different coordination modes to the transition metal. Hence, the destabilized O^- species can form O–O bonds and move from a η^1- to η^2-type coordination mode, then reducing the transition metal. This mechanism is here highly favoured by the presence of Sn^{4+}, which does not affect hybridization, as opposed to other 3d metals encountered in these high-capacity electrodes (Mn, for instance).

In addition to unravelling the fundamental mechanisms of these high-capacity electrodes, this work is also important for practical applications despite the use of Ru. We have shown that by adding a spectator cation, we can achieve good cycle life and eliminate the voltage decay on cycling observed in the Li-rich NMC composites or Ru/Mn compounds. The present finding also provides a final answer to the long debates about the need for composite as opposed to single phases in high-capacity electrodes, as one single phase is sufficient to make it. Besides, the replacement of Mn by Sn in the Li-rich NMC materials could be a valuable option to improve their cycle life. To combat similar issues, other tetravalent metals, as we are experiencing at present, are equally worthy of consideration provided they offer the proper compromise in terms of electropositive character, ionic radius and coordination. More

833

importantly, this work opens new fertile ground in the search for new high-capacity electrodes, provided that we widely use chemistry to pair active and non-active cations and we select the ones that will give a decent electronic conductive matrix. Band-structure calculations could be used as a guide to anticipate energy levels and also serve to predict when hybridization will occur, as long as we define band energy referential. This will imply working not only on the transition metal but also on the ligands that can act as reductive agents to regenerate the transition-metal oxidation state during the oxidation process. Furthermore, from a material's prospective, we should recall that the Li_2MO_3 family is rich and still largely unexplored. Similar phases with the general formula $Li_4MM'O_6$ exist or can be discovered as long as the sum of the oxidation states of M and M' is equal to eight. As for IV–IV, III–V and II–VI semiconductors, the $Li_4Ru^{4+}Ti^{4+}O_6$, $Li_4Fe^{3+}Sb^{5+}O_6$ and $Li_4Cd^{2+}Te^{6+}O_6$ phases do exist[44] and many others can be made, including sodium-based ones, thereby opening a wide window within the periodic table from which it will be relevant to find the best combination having the proper elements in terms of sustainability. We hope that the battery community will follow on this promising path.

Methods

Synthesis of $Li_2Ru_{1-y}Sn_yO_3$ ($0 \leqslant y \leqslant 1$). Proper amounts of RuO_2 (Sigma-Aldrich 99.9%) and SnC_2O_4 (Sigma-Aldrich 98%) were homogenized, using a mortar and pestle for 20 min and then ball milled for 40 min with a 10%wt excess of Li_2CO_3 (Sigma-Aldrich, purity 99.0%) to compensate its volatilization at high temperature. The resultant mixture was heated in an alumina crucible at 800 °C for 6 h followed by heating at 900 °C for 12 h and at 1,100 °C for 12 h with intermediate grindings for 40 min. The furnace heating and cooling rate was maintained at 2 °C min⁻¹.

XRD. XRD patterns were recorded using two separate Bruker D8 diffractometers. The first one was equipped with a Co-K_α radiation source ($\lambda_1 = 1.78897$ Å, $\lambda_2 = 1.79285$ Å) with a Vantec detector whereas the other used a Cu-K_α radiation source ($\lambda_1 = 1.54056$ Å, $\lambda_2 = 1.54439$ Å) with a LynxEye detector. Both were operated at 40 kV and 40 mA. All powder patterns were refined using the Rietveld method as implemented in the FullProf program[45]. For in situ studies, a stainless-steel Swagelok-style cell with an X-ray-transparent Be window was employed. An aluminium foil was placed between the cathode material (mixed with 15wt% carbon) and the Be window, to prevent Be oxidation at high operating voltages.

Electrochemical insertion/extraction of Li⁺. Electrochemical tests versus Li were done in Swagelok-type cells. The cells were assembled in an argon-filled glove box, using a Li metal disc as the negative electrode, and a Whatman GF/D borosilicate glass fibre sheet saturated with a 1 M $LiPF_6$ solution in a mixture of ethylene carbonate, propylene carbonate and dimethyl carbonate in a 1:1:3 ratio by weight (LP100). The working electrodes were typically made by ball milling powders of $Li_2Ru_{1-y}Sn_yO_3$ with 10% in mass of carbon Ketjen black (or SP) for 15 min. Usually, 6–8 mg of the mixed powders was used per cell. The mechanical mixing was performed under an argon atmosphere using a Spex-800 mixer mill. Galvanostatic charge–discharge tests were conducted at 20 °C using a Mac-Pile or a VMP system (Biologic S.A.) operating in galvanostatic mode. Unless otherwise specified, the cells were typically cycled between 4.6 and 2 V versus Li⁺/Li⁰ at 1 Li⁺ exchanged per 10 h (C/10). The power rate was defined using a 'signature curve' using the same protocol as reported previously[46].

Electron microscopy. TEM pictures were obtained using an FEI Tecnai F20 S-Twin electron microscope operating at 200 kV and fitted with an EDAX energy-dispersive spectrometer. $Li_xRu_{1-y}Sn_yO_3$ samples were deposited on a TEM holey carbon copper grid.

EPR spectra. EPR spectra were recorded respectively at room temperature and 4 K with a Bruker ELEXSYS E580 spectrometer. Microwave power and modulation amplitude were respectively set to 5 mW and 5 G. All of the spectra were normalized with the weight of material analysed to compare the intensity of all paramagnetic species. Although Ru-based oxides exhibit a complex magnetic behaviour[47], a classical double integration procedure was successfully adopted to deduce the quantitative amount of peroxo-like species.

Mössbauer spectroscopy. Room-temperature ¹¹⁹Sn Mössbauer spectra were recorded in transmission geometry in the constant acceleration mode and with a Ca¹¹⁹SnO₃ source with normal activity of 925 MBq. The velocity scale (± 7 mm s⁻¹) was calibrated at room temperature with α-Fe foil. The absorbers were prepared from 10 mg cm⁻² of powder. The hyperfine parameters IS (isomer shift) and QS (quadrupole splitting) were determined by fitting Lorentzian

lines to the experimental data. The isomer shifts values are calculated with respect to that of $BaSnO_3$.

XPS data collection and analysis. XPS measurements were carried out with a Kratos Axis Ultra spectrometer, using a focused monochromatized Al K_α radiation (1,486.6 eV). The XPS spectrometer was directly connected through a transfer chamber to an argon dry box, to avoid moisture/air exposure of the samples. For the Ag$3d_{5/2}$ line the full-width at half-maximum was 0.58 eV under the recording conditions. The analysed area of the samples was 300×700 μm². Peaks were recorded with a constant pass energy of 20 eV. The pressure in the analysis chamber was around 5×10^{-9} mbar. Short acquisition time spectra were recorded before and after each normal experiment to check that the samples did not suffer from degradation during the measurements. The binding energy scale was calibrated from the hydrocarbon contamination using the $C1s$ peak at 285.0 eV. Core peaks were analysed using a nonlinear Shirley-type background. The peak positions and areas were optimized by a weighted least-squares fitting method using 70% Gaussian, 30% Lorentzian line shapes. Quantification was performed on the basis of Scofield's relative sensitivity factors.

DFT+U calculations. Calculations were performed using the plane-wave DFT code from the Vienna Ab initio Simulation Package[48]. All calculations were performed within the generalized gradient approximation and the Perdew–Burke–Ernzerhof potential for exchange and correlation energy[49]. The plane-wave energy cutoff was set to 600 eV and the Brillouin zone integration was done in a k-point grid distributed as uniformly as possible. All atom coordinates and lattice parameters were fully relaxed using conjugate gradient energy minimization until the forces acting on each atom were less than 5×10^{-3} eV Å⁻². All structures were investigated within the spin-polarized DFT+U framework, using $U_{eff} = U - J = 4$ eV for Ru ($J = 1.0$ eV).

Oxygen analysis. Electrochemical experiments were performed with a VMP3 (Biologic S.A.) potentiostat. Mass spectrometry measurements were made with a Pfeiffer Vacuum OmniStar GDS 320 01 with a mass range of 1–100 amu. Two electrode cells for gas analysis consisted of a 32-mm-diameter, 4-mm-thick EP-70 O-ring sandwiched between two 38.1-mm-diameter stainless-steel current collectors, one of which was drilled with 1.6 mm diameter Valco Instruments internal compression fittings for gas access. Tests on blank cells were done with 5 mg of Carbon Super P (Csp). Cells contained ~9 mg of active material with 10% Csp cathodes, 150 μl of LP100 electrolyte, a 19-mm-diameter Whatman separator (grade GF/D, 12.7 mm diameter), and an 11.1-mm-diameter Li disc, and were cycled at a rate of C/20. The entire electrochemical mass spectrometry system was He-leak-tested using the mass spectrometer. Cells were sampled and purged once every 16 min for gas analysis, with an Ar environment used for charging, and two- and four-hours open circuit voltage dwells after discharge and charge, respectively, to thoroughly change the gas environment between half-cycles.

Pressure cell. The cell consisted of a modified two-electrode Swagelok-type airtight fixture using a stainless-steel rod (working-electrode side) and a 10 cm tube (counter-electrode side) current collector. The stainless-steel tube was connected through a side arm to an Omegadyne PX329-030A5V pressure sensor with a pressure range of 0–30 PSI. Cells were kept at a constant 30 °C using a Binder incubator. Cells contained ~9 mg of active material with 10% Csp cathodes, 100 μl of LP100 electrolyte, a 19-mm-diameter Whatman separator (grade GF/D, 12.7 mm diameter), and an 11.1-mm-diameter Li disc, and were cycled at a rate of C/20. All cell construction was carried out in an argon-filled glove box where both H_2O and O_2 levels were kept below 1 ppm. Before conducting the electrochemical testing, the cell was filled with 1.5 atm of pure argon (U.H.P. grade). The charge was followed by a 4 h open circuit voltage to verify that the cell was not leaking.

References

1. Armand, M. & Tarascon, J. M. Building better batteries. *Nature* **451**, 652–657 (2008).
2. Tarascon, J. M. & Armand, M. Issues and challenges facing rechargeable lithium batteries. *Nature* **414**, 359–367 (2001).
3. Ohzuku, T. & Makimura, Y. Layered lithium insertion material of LiCo$_{1/3}$Ni$_{1/3}$Mn$_{1/3}$O$_2$ for lithium-ion batteries. *Chem. Lett.* **30**, 642–643 (2001).
4. Yoshizawa, H. & Ohzuku, T. An application of lithium cobalt nickel manganese oxide to high-power and high-energy density lithium-ion batteries. *J. Power Sources* **174**, 813–817 (2007).
5. Thackeray, M. M., David, W. I. F., Bruce, P. G. & Goodenough, J. B. Lithium insertion in Manganese spinels. *Mater. Res. Bull.* **18**, 461–472 (1983).
6. Barpanda, P. *et al.* A 3.90 V iron-based fluorosulphate material for lithium-ion batteries crystallizing in the triplite structure. *Nature Mater.* **10**, 772–779 (2011).
7. Padhi, A. K., Nanjundaswamy, K. S. & Goodenough, J. B. Phospho-olivines as positive-electrode materials for rechargeable lithium batteries. *J. Electrochem. Soc.* **144**, 1188–1194 (1997).

8. Johnson, C. S. *et al.* The significance of the Li₂MnO₃ component in 'composite' xLi_2MnO_3. $(1 − x)LiMn_{0.5}Ni_{0.5}O_2$ electrodes. *Electrochem. Commun.* **6,** 1085–1091 (2004).

9. Johnson, C. S., Li, N. C., Lefief, C., Vaughey, J. T. & Thackeray, M. M. Synthesis, characterization and electrochemistry of lithium battery electrodes: xLi_2MnO_3. $(1 − x)LiMn_{0.333}Ni_{0.333}Co_{0.333}O_2$ ($0 < x < 0.7$). *Chem. Mater.* **20,** 6095–6106 (2008).

10. Thackeray, M. M., Johnson, C. S., Vaughey, J. T., Li, N. & Hackney, S. A. Advances in manganese-oxide 'composite' electrodes for lithium-ion batteries. *J. Mater. Chem.* **15,** 2257–2267 (2005).

11. Thackeray, M. M., Kang, S. H., Johnson, C. S., Vaughey, J. T. & Hackney, S. A. Comments on the structural complexity of lithium-rich $Li_{1+x}M_{1−x}O_2$ electrodes (M = Mn, Ni, Co) for lithium batteries. *Electrochem. Commun.* **8,** 1531–1538 (2006).

12. Hodeau, J. L., Marezio, M., Santoro, A. & Roth, R. S. Neutron profile refinement of the structures of Li_2SnO_3 and Li_2ZrO_3. *J. Solid State Chem.* **45,** 170–179 (1982).

13. James, A. & Goodenough, J. B. Structure and bonding in lithium ruthenate, Li_2RuO_3. *J. Solid State Chem.* **74,** 287–294 (1988).

14. Armstrong, A. R. *et al.* Demonstrating oxygen loss and associated structural reorganization in the lithium battery cathode $LiNi_{0.2}Li_{0.2}Mn_{0.6}O_2$. *J. Amer. Chem. Soc.* **128,** 8694–8698 (2006).

15. Koga, H. *et al.* Reversible oxygen participation to the redox processes revealed for $Li_{1.20}Mn_{0.54}Co_{0.13}Ni_{0.13}O_2$. *J. Electrochem. Soc.* **160,** A786–A792 (2013).

16. Koga, H. *et al.* Different oxygen redox participation for bulk and surface: A possible global explanation for the cycling mechanism of $Li_{1.20}Mn_{0.54}Co_{0.13}Ni_{0.13}O_2$. *J. Power Sources* **236,** 250–258 (2013).

17. Sathiya, M. *et al.* High performance $Li_2Ru_{1−y}Mn_yO_3$ ($0.2 < y < 0.8$) cathode materials for rechargeable lithium-ion batteries: Their understanding. *Chem. Mater.* **25,** 1121–1131 (2013).

18. Xiao, R. J., Li, H. & Chen, L. Q. Density functional investigation on Li_2MnO_3. *Chem. Mater.* **24,** 4242–4251 (2012).

19. Mori, D. *et al.* Synthesis, phase relation and electrical and electrochemical properties of ruthenium-substituted Li_2MnO_3 as a novel cathode material. *J. Power Sources* **196,** 6934–6938 (2011).

20. Tarakina, N. V. *et al.* Investigation of stacking disorder in Li_2SnO_3. *Z. Kristall.* 375–380 (2011).

21. Shannon, R. D. Revised effective ionic-radii and systematic studies of interatomic distances in halides and chalcogenides. *Acta Crystallogr. Sec. A* **32,** 751–767 (1976).

22. Kobayashi, H., Kanno, R., Kawamoto, Y., Tabuchi, M. & Nakamura, O. Physical properties of the de-lithiated $Li_{2−x}RuO_3$ with the layered structure. *Solid State Ion.* **86-8,** 859–863 (1996).

23. Teo, L. P., Buraidah, M. H., Nor, A. F. M. & Majid, S. R. Conductivity and dielectric studies of Li_2SnO_3. *Ionics* **18,** 655–665 (2012).

24. Park, S. H., Sato, Y., Kim, J. K. & Lee, Y. S. Powder property and electrochemical characterization of Li_2MnO_3 material. *Mater. Chem. Phys.* **102,** 225–230 (2007).

25. Gu, M. *et al.* Formation of the spinel phase in the layered composite cathode used in Li-ion batteries. *ACS Nano* **7,** 760–767 (2013).

26. Selwyn, L. S., McKinnon, W. R., Dahn, J. R. & Lepage, Y. Local environment of Li intercalated in $Mo_6Se_zS_{8−z}$ as probed using electrochemical methods. *Phys. Rev. B* **33,** 6405–6414 (1986).

27. Yabuuchi, N., Yoshii, K., Myung, S. T., Nakai, I. & Komaba, S. Detailed studies of a high-capacity electrode material for rechargeable batteries, $Li_2MnO_3–LiCo_{1/3}Ni_{1/3}Mn_{1/3}O_2$. *J. Amer. Chem. Soc.* **133,** 4404–4419 (2011).

28. Dulac, J. Spinel compounds between ruthenium oxide RuO_2 and some Transition Metal oxides. *Bull. Soc. Fr. Mineral. Cr.* **92,** 487–488 (1969).

29. Nozik, A. J. Optical and electrical properties of Cd_2SnO_4—A defect semiconductor. *Phys. Rev. B* **6,** 453–459 (1972).

30. Singh, P. *et al.* Electronic structure, electrical and dielectric properties of $BaSnO_3$ below 300 K. *Jpn. J. Appl. Phys.* **47,** 3540–3545 (2008).

31. Mouyane, M., Womes, M., Jumas, J. C., Olivier-Fourcade, J. & Lippens, P. E. Original electrochemical mechanisms of $CaSnO_3$ and $CaSnSiO_5$ as anode materials for Li-ion batteries. *J. Solid State Chem.* **184,** 2877–2886 (2011).

32. Manju, U., Awana, V. P. S., Kishan, H. & Sarma, D. D. X-ray photoelectron spectroscopy of superconducting $RuSr_2Eu_{1.5}Ce_{0.5}Cu_2O_{10}$ and nonsuperconducting $RuSr_2EuCeCu_2O_{10}$. *Phys. Rev. B* **74,** 245106 (2006).

33. Lu, M. F., Deng, X. L., Waerenborgh, J. C., Wu, X. J. & Meng, J. Redox chemistry and magnetism of $LaSrM_{0.5}Ru_{0.5}O_{4+/−δ}$ (M = Co, Ni and Zn) Ruddlesden–Popper phases. *Dalton Trans.* **41,** 11507–11518 (2012).

34. Dupin, J. C., Gonbeau, D., Vinatier, P. & Levasseur, A. Systematic XPS studies of metal oxides, hydroxides and peroxides. *Phys. Chem. Chem. Phys.* **2,** 1319–1324 (2000).

35. Fukuzumi, S. & Ohkubo, K. Quantitative evaluation of Lewis acidity of metal ions derived from the *g* values of ESR spectra of superoxide: Metal ion complexes in relation to the promoting effects in electron transfer reactions. *Chem.-Eur. J.* **6,** 4532–4535 (2000).

36. Rouxel, J. The importance of anions in redox-type chimie douce. *Mol. Cryst. Liq. Cryst. Sci. Technol. Sect. A* **310,** 1–4 (1998).

37. Rouxel, J. Anion–cation redox competition and the formation of new compounds in highly covalent systems. *Chem.-Eur. J.* **2,** 1053–1059 (1996).

38. Rouxel, J. Design and chemical reactivity of low dimensional solids—some soft chemistry routes to new solids. *Acs Symp. Ser.* **499,** 88–113 (1992).

39. Bichat, M. P. *et al.* Redox-induced structural change in anode materials based on tetrahedral $(MPn_4)^{x−}$ transition metal pnictides. *Chem. Mater.* **16,** 1002–1013 (2004).

40. Ceder, G. *et al.* Identification of cathode materials for lithium batteries guided by first-principles calculations. *Nature* **392,** 694–696 (1998).

41. Tarascon, J. M. *et al.* In situ structural and electrochemical study of $Ni_{1−x}Co_xO_2$ metastable oxides prepared by soft chemistry. *J. Solid State Chem.* **147,** 410–420 (1999).

42. Graetz, J., Ahn, C. C., Yazami, R. & Fultz, B. An electron energy-loss spectrometry study of charge compensation in $LiNi_{0.8}Co_{0.2}O_2$. *J. Phys. Chem. B* **107,** 2887–2891 (2003).

43. Li, H., Wang, Z., Chen, L. & Huang, X. Research on advanced materials for Li-ion batteries. *Adv. Mater.* **21,** 4593–4607 (2009).

44. Zvereva, E. A. *et al.* A new layered triangular antiferromagnet Li_4FeSbO_6: Spin order, field-induced transitions and anomalous critical behavior. *Dalton Trans.* **42,** 1550–1566 (2013).

45. Rodriguez-Carvajal, J. Recent advances in magnetic-structure determination by neutron powder diffraction. *Physica B* **192,** 55–69 (1993).

46. Doyle, M., Newman, J. & Reimers, J. A quick method of measuring the capacity versus discharge rate for a dual lithium-ion insertion cell undergoing cycling. *J. Power Sour.* **52,** 211–216 (1994).

47. Cava, R. J. Schizophrenic electrons in ruthenium-based oxides. *Dalton Trans.* 2979–2987 (2004).

48. Kresse, G. & Furthmuller, J. Efficient iterative schemes for *ab initio* total-energy calculations using a plane-wave basis set. *Phys. Rev. B* **54,** 11169–11186 (1996).

49. Perdew, J. P., Burke, K. & Ernzerhof, M. Generalized gradient approximation made simple. *Phys. Rev. Lett.* **77,** 3865–3868 (1996).

50. Dedryvere, R. *et al.* Electrode/electrolyte interface reactivity in high-voltage spinel $LiMn_{1.6}Ni_{0.4}O_4/Li_4Ti_5O_{12}$ lithium-ion battery. *J. Phys. Chem. C* **114,** 10999–11008 (2010).

Acknowledgements

Author contributions

M.S., K.R., C.P.L. and A.S.P. carried out the synthesis, M.S. and J-M.T. conducted the electrochemical work and J-M.T. designed the research approach; G.R. analysed the crystal structures and diffraction patterns; H.V. collected and analysed the EPR spectra; M.T.S. collected and analysed the Mössbauer data; D.F. and D.G. collected and analysed the XPS spectra; W.W. performed the pressure cell experiments: M.B.H. and L.D. carried out the TEM studies: M-L.D. conducted the DFT calculations and developed the theoretical framework; M-L.D., G.R. and J-M.T. wrote the manuscript and all authors discussed the experiments and final manuscript.

Additional information

Competing financial interests

The authors declare no competing financial interests.